

Article

Silica-Supported Assemblage of Cu^{II} Ions with Carbon Dots for Self-Boosting and Glutathione-Induced ROS Generation

Olga Bochkova ^{1,2,*}, Alexey Dovjenko ², Rustem Zairov ¹, Kirill Kholin ³, Rinata Biktimirova ², Svetlana Fedorenko ¹, Irek Nizameev ¹, Artem Laskin ², Alexandra Voloshina ¹, Anna Lyubina ¹, Syumbelya Amerhanova ¹, Amina Daminova ⁴, Vladimir Evtugyn ⁴, Tatiana Gerasimova ¹ and Asiya Mustafina ¹

- ¹ Arbuzov Institute of Organic and Physical Chemistry, FRC Kazan Scientific Center of RAS, Arbuzov Str., 8, 420088 Kazan, Russia; rustem02@yandex.ru (R.Z.); svetlana.fedorenko@yahoo.com (S.F.); irek.rash@gmail.com (I.N.); sobaka-1968@mail.ru (A.V.); alyubina@gmail.com (A.L.); syumbelya07@mail.ru (S.A.); tatyanaagr@gmail.com (T.G.); asiyamust@mail.ru (A.M.)
- ² Alexander Butlerov Institute of Chemistry, Kazan (Volga Region) Federal University, 18 Kremlyovskaya Str., 420008 Kazan, Russia; aleksej_dovghenko@mail.ru (A.D.); rinatuci@mail.ru (R.B.); artemka166@mail.ru (A.L.)
- ³ Institute of Radio Electronics, Photonics and Digital Technologies, Kazan National Research Technical University Named after A.N. Tupolev-KAI, 10, K. Marx Str., 420111 Kazan, Russia; kholin06@mail.ru
- ⁴ Interdisciplinary Center for Analytical Microscopy, Kazan (Volga Region) Federal University, 9 Paris Commune Str., 420008 Kazan, Russia; aminochka_88@mail.ru (A.D.); VGEvtjugin@kpfu.ru (V.E.)
- * Correspondence: o.d.bochkova@mail.ru

Abstract: The present work introduces coordinative binding of Cu^{II} ions with both amino-functionalized silica nanoparticles (SNs) and green-emitting carbon dots (CDs) as the prerequisite for the Cu^{II}-assisted self-assembly of the CDs at the surface of the SNs. The produced composite SNs exhibit stable in time stimuli-responsive green fluorescence derived from the Cu^{II}-assisted assemblage of CDs. The fluorescence response of the composite SNs is sensitive to the complex formation with glutathione (GSH), enabling them to detect it with the lower limit of detection of 0.15 μM. The spin-trap-facilitated electron spin resonance technique indicated that the composite SNs are capable of self-boosting generation of ROS due to Cu^{II}→Cu^I reduction by carbon in low oxidation states as a part of the CDs. The intensity of the ESR signals is enhanced under the heating to 38 °C. The intensity is suppressed at the GSH concentration of 0.35 mM but is enhanced at 1.0 mM of glutathione, while it is suppressed once more at the highest intracellular concentration level of GSH (10 mM). These tendencies reveal the concentrations optimal for the scavenger or reductive potential of GSH. Flow cytometry and fluorescence and confocal microscopy methods revealed efficient cell internalization of SNs-NH₂-Cu^{II}-CDs comparable with that of “free” CDs.

Keywords: carbon dots; silica nanoparticles; chemodynamic therapy; reactive oxygen species generation; glutathione; cellular marking



Citation: Bochkova, O.; Dovjenko, A.; Zairov, R.; Kholin, K.; Biktimirova, R.; Fedorenko, S.; Nizameev, I.; Laskin, A.; Voloshina, A.; Lyubina, A.; et al. Silica-Supported Assemblage of Cu^{II} Ions with Carbon Dots for Self-Boosting and Glutathione-Induced ROS Generation. *Coatings* **2022**, *12*, 97. <https://doi.org/10.3390/coatings12010097>

Academic Editor: Ajay Vikram Singh

Received: 13 December 2021

Accepted: 11 January 2022

Published: 15 January 2022

Publisher's Note: MDPI stays neutral with regard to jurisdictional claims in published maps and institutional affiliations.



Copyright: © 2022 by the authors. Licensee MDPI, Basel, Switzerland. This article is an open access article distributed under the terms and conditions of the Creative Commons Attribution (CC BY) license (<https://creativecommons.org/licenses/by/4.0/>).

1. Introduction

Silica nanoparticles (SNs) are convenient nanobeads for both molecular and nanosized dopants, which can be either included in the silica matrix or deposited onto the silica surface through the cooperative effect of multiple noncovalent interactions [1–4]. It is worth noting that a surface modification of SNs is of greater impact on their cellular uptake and sensing than the inclusive modification of SNs. Thus, the present work represents noncovalent surface decoration of SNs by green-emissive carbon dots (CDs) facilitated by coordination bonds as a route for developing a composite nanomaterial combining functional properties derived from both metal ions and CDs.

Emissive carbon dots (CDs) have gained much attention as the basis for sensing [5,6]. Thus, the present work represents an assemblage of green-emissive carbon dots (CDs) facilitated by coordination bond as a mode of noncovalent surface decoration of SNs aimed

at developing a composite nanomaterial for sensing, imaging and reactive oxygen species (ROS) generation. The claimed aim requires specific metal ions and functional groups at the surface of SNs, which are able to (1) form efficient coordination bonds to provide the assemblage of CDs at the surface of SNs, (2) be labile to give a quick response on biorelevant substrates and (3) be redox-active to generate ROS in cell cytoplasm.

The use of Cu^{II} ions to form coordinative bonds facilitating adsorption of the CDs derives from their well-known outstanding coordination ability represented by the Irving–Williams series. The high efficiency of the coordination binding of copper ions with amino groups can be applied as a tool to modify the functional properties of a material, as it has been successfully applied in the modification of room-temperature multiferroicity of polyaniline-based material [7]. The amino-modified SNs bearing multiple amino groups at their surface have been already documented as the nanobeads for Cu^{II} ions [8–11]. The present work introduces Cu^{II} -supported coordinative bonds at a silica/water interface of the amino-modified SNs as the driving force of embedding of green-emitting carbon dots (CDs) onto the SNs. Unlike the previously reported doping of the CDs into SNs or mesoporous SNs [12,13], the combination of Cu^{II} ions with fluorescent CDs on amino-modified SNs is the prerequisite for the development of the stimuli-responsive assemblage of CDs on the surface of SNs. Thus, the applicability of the developed composite SNs in sensing is introduced herein.

The ability of Cu^{II} -containing nanomaterials to generate ROS through Fenton-like reactions in the presence of some reductants exemplified by cytosolic glutathione [14–20] is of great biomedical importance, since the ROS generation, in turn, is the well-known basis for chemodynamic therapy (CDT) as an alternative route for cancer cell treating [21–24]. However, the reductive capacity of cytosolic GSH is the well-known reason for its radical scavenger function within cells [25]. It is also worth noting that the reductive effect of GSH on Cu^{II} -containing nanomaterials interferes with its ability to coordinate Cu^{II} ions, which results in specific concentration requirements for the significant $\text{Cu}^{\text{II}} \rightarrow \text{Cu}^{\text{I}}$ reduction [14]. Thus, the present work is aimed at highlighting the complex formation of the composite nanomaterial with glutathione (GSH) through its sensing ability, in turn, derived from Cu^{II} -CDs combination at the surface of the amino-modified SNs.

It has been already documented that the red-emitting CDs being combined with Cu^{II} and Fe^{II} ions provide the irradiation-induced [15] and hydrogen peroxide induced [26] CDT effects. However, the origin of the CDT generated by Cu^{II} -CDs in the presence of cytosolic GSH is not well understood. The factors responsible for the ROS generation by the developed composite SNs combining Cu^{II} and CDs on their surface are highlighted with the use of electron spin spectroscopy (ESR) technique facilitated by 5,5-dimethyl-pyrroline N-oxide (DMPO) as the spin trap. In particular, the impact of different concentration levels of GSH on ROS generation is also revealed by means of the ESR technique.

The present work also introduces the stability of the Cu^{II} -facilitated assembly of the CDs at the surface of the amino-modified SNs and their applicability in cellular marking. Therefore, flow cytometry, cell viability and fluorescence and confocal microscopy measurements are also introduced for revealing the potential of the developed composite SNs in cellular imaging.

2. Materials and Methods

Commercial chemicals tetraethyl orthosilicate (TEOS, 98%), ammonium hydroxide (28%–30%), n-hexanol (98%), cyclohexane (99%), hexane (99%), acetone (99%), 3-aminopropyltriethoxysilane (APTES, 99%), and β -alanine were purchased from Acros Organics (Thermo Fisher Scientific, Waltham, MA, USA). Triton X-100 (98%), copper (II) chloride (97%), citric acid (99%), urea (99%), 5,5-dimethyl-pyrroline N-oxide (DMPO), 4',6-diamidino-2-phenylindole dihydrochloride (DAPI), propidium iodide, fluorescamine and L-glutathione reduced (GSH, 98%) were purchased from Sigma-Aldrich (St. Louis, MO, USA). L-Cysteine (for biochemistry) was purchased from Merck (Darmstadt, Germany).

Ethanol was purified by distillation under atmospheric pressure, whereas TEOS was distilled under reduced pressure. All other chemicals were used as received without further purification.

The synthesis of carbon quantum dots was carried out by thermolysis of urea citrate [27]. Citric acid and urea in a ratio of 1:5 were refluxed for two hours at a temperature of 155 °C (with temperature fluctuations of 3 °C). Through synthesis, the color of the melt changed from transparent to dark brown. After the completion of the reaction, the product was dissolved in excess water, filtered using a filter membrane (0.22 µm) and dried at room temperature.

Amino-modified silica nanoparticles (SNs-NH₂) and silica nanoparticles (SNs) were synthesized in accordance with the previously published procedures [28,29].

The adsorption of Cu^{II} onto SNs and SNs-NH₂ was performed as follows: aqueous colloids of SNs or SNs-NH₂ (2.8 gL⁻¹) were mixed with CuCl₂ (5 mM) using a Multi Reax shaker set-up (Heidolph, Schwabach, Germany) for 1 day. Next, the mixture was left to stay for 2 days, after which the SNs were separated by centrifugation (15 min, 15,000 rpm, 4 °C) and washed 3 times to remove unbound Cu(II) ions. The initial white silica nanoparticles became blue.

For adsorption of CDs (10 gL⁻¹) onto SNs-NH₂-Cu^{II} or SNs-NH₂ and SNs-Cu^{II} (0.5 gL⁻¹), all components were mixed using a shaker set-up for 1 day. Afterward, the treated SNs were separated by centrifugation (15 min, 15,000 rpm, 4 °C) and triply washed. Concentration ratio of SNs to CDs equal to 1:20 and 24 h shaking were selected as optimal conditions for obtaining a high-luminescent and stable nanoparticle system. Obtained colloids were dark brown.

The Transmission electron microscopy (TEM) images were obtained by means of Hitachi HT7700 (Japan, Tokyo, Japan) at an accelerating voltage of 100 kV.

Cu and Si were identified in the solutions using simultaneous inductively coupled plasma optical emission spectrometry (ICP-OES) model iCAP 6300 DUO by Varian Thermo Scientific Company (Waltham, MA, USA) equipped with a Charge Injection Devices (CID) detector. This spectrometer enables the simultaneous measurement of peak heights within the 166 to 867 nm range. The optical resolution is less than 0.007 to 200 nm. The working frequency is 27.12 MHz. Together, the radial and axial view configurations enable optimal peak height measurements with suppressed spectral noises. Concentrations of Cu and Si ions were determined, respectively, by the 327.396 and 251.611 nm spectral lines.

Powdered samples were characterized by Ultraviolet-visible/diffuse reflectance (UV-Vis/DR) technique using a Jasco V-650 spectrophotometer (Jasco International Co. Ltd., Tokyo, Japan) equipped with an integrating sphere accessory for diffuse reflectance spectra acquisition. BaSO₄ powder was used as the reference for baseline correction.

UV-Vis spectra were recorded on Specord^R50 Plus (Analytikjena, Jena, Germany). SNs dispersions were ultrasonicated within 10 min before use.

Dynamic light scattering (DLS) measurements were performed by means of the Malvern Mastersize 2000 particle analyzer. A He-Ne laser operating at 633 nm wavelength and emitting vertically polarized light was used as a light source. The measured autocorrelation functions were analyzed by Malvern DTS software (version 7.10) and the second-order cumulant expansion methods. The effective hydrodynamic radius (R_H) was calculated by the Einstein–Stokes relation from the first cumulant: $D = k_B T / 6\pi\eta R_H$, where D is the diffusion coefficient, k_B is the Boltzmann constant, T is the absolute temperature and η is the viscosity. The diffusion coefficient was measured at least three times for each sample. The average error in these experiments is approximately 4%. The samples for DLS study were prepared from deionized water, sonicated for 10 min and equilibrated at 25.0 ± 0.1 °C before DLS and zeta-potential measurements.

The steady-state emission spectra were recorded on a fluorescence spectrophotometer Hitachi F-7100 (Japan, Tokyo, Japan) with stigmatic concave diffraction grating. All samples were ultrasonicated for 10 min before measurements. $\lambda_{ex} = 420$ nm, slit = 5 nm, voltage = 700 mV; C (CDs) = 0.005 gL⁻¹; C (SNs-NH₂-Cu^{II}-CDs) = 0.05 gL⁻¹.

The fluorescence procedure with the use of fluorescamine (Figure S1) was used for quantitative analysis of amino groups on the surface of silica nanoparticles [30].

Limit of detection was evaluated by the following equation: $LOD = 3\sigma/S$, where S is slope and σ is standard deviation ($\sigma = \sqrt{\frac{\sum_{i=1}^n (x_i - \bar{x})^2}{n}}$).

The ESR measurements were carried out on the ELEXSYS E500 ESR spectrometer of the X-range (Bruker, Billerica, MA, USA). ESR spectra were simulated using the WinSim program (developed by NIEHS, version 0.96). The irradiation of the samples was carried out by light-emitting diode (405 nm) at a distance of 10 cm from the light source. The samples were aqueous (used deionized water) solutions of 0.1 M DMPO in the presence of analyzed objects. Temperature in the ESR spectrometer cavity was set using the ER 4131VT Variable Temperature System (Bruker, Billerica, MA, USA).

Cytotoxic effects of samples on human cancer and normal cells were estimated by means of the multifunctional Cytell Cell Imaging system (GE Health Care Life Science, Uppsala, Sweden) using the Cell Viability Bio App (version 3.6.7.19) which precisely counts the number of cells and evaluates their viability from fluorescence intensity data [31]. The M-HeLa clone 11 human, epithelioid cervical carcinoma, strain of HeLa, clone of M-HeLa; WI-38 VA-13 cell culture, subline 2RA (human embryonic lung), from the Type Culture Collection of the Institute of Cytology (Russian Academy of Sciences, Moscow, Russia); and Chang Liver cell line (Human liver cells) from N. F. Gamaley Research Center of Epidemiology and Microbiology were used in the experiments. The cells were cultured in a standard Eagle's nutrient medium manufactured at the Chumakov Institute of Poliomyelitis and Virus Encephalitis (PanEco company, Tokyo, Japan) and supplemented with 10% fetal calf serum and 1% nonessential amino acids. The cells were plated into a 96-well plate (Eppendorf, Hamburg, Germany) at a concentration of 1×10^5 cells mL^{-1} , 150 μL of medium per well, and cultured in a CO_2 incubator at 37 °C. Twenty-four hours after seeding the cells into wells, the compound under study was added at a preset dilution, 150 μL to each well. The dilutions of the compounds were prepared immediately in nutrient media; 5% dimethyl sulfoxide (DMSO), which does not induce the inhibition of cells at this concentration, was added for better solubility. The experiments were repeated three times. Intact cells cultured in parallel with experimental cells were used as a control.

The uptake of SNs-NH₂-Cu^{II}-CDs by M-HeLa cells was analyzed using flow cytometry (Guava easy Cyte 8HT, Austin, TX, USA). Flow cytometry was used to generate statistics on the uptake of the test complex by cancer cells. Untreated cells were used as negative control. M-HeLa cells at 1×10^5 cells/well were plated into 6-well plates to a final volume of 2 mL. After a 24 h incubation, solution of SNs-NH₂-Cu^{II}-CDs (0.5 gL^{-1}) was added to the M-HeLa cells and incubated for 24 h in a CO_2 incubator.

Fluorescence microscopy images were obtained by using a Nikon Eclipse Ci-S fluorescence microscope. (Nikon, Tokyo, Japan) at 1000 \times magnification. M-HeLa cells at 1×10^5 cells/well in a final volume of 2 mL were seeded into 6-well coverslip plates at the bottom of each well. After 24 h of incubation, solutions of the studied SNs-NH₂-Cu^{II}-CDs (0.5 gL^{-1}) were added to the wells and cultured for 24 h in a CO_2 incubator. Then, M-HeLa cells were fixed and stained with DAPI (blue, cell nucleus staining).

Confocal laser microscopy images of the control M-HeLa cell lines and cells, incubated with SNs-NH₂-Cu^{II}-CDs were obtained by CLMS on an inverted Carl Zeiss LSM 780 confocal laser-scanning microscope (Carl Zeiss, Jena, Germany). M-HeLa cells in an amount of 1×10^5 cells/well in a final volume of 2 mL were seeded in 6-well plates with coverslips at the bottom of each well. After 24 h of incubation, SNs-NH₂-Cu^{II}-CDs at the concentration of 0.5 gL^{-1} were added to the wells and incubated for 24 h in a CO_2 incubator. Then, the samples were simultaneously stained with DAPI (blue fluorescent) in the amount of 1% of the volume of sample medium for 15 min. The nanoparticles' luminescence was detected in the green channel. Untreated cells were used as negative control.

3. Results and Discussion

3.1. Synthesis and Characterization of the Hybrid SNs

The amino decoration of SNs was fulfilled within the one-pot synthetic approach; the produced SNs became the nanobeads for Cu^{II} ions, which were embedded through coordinative bonds with amino groups at the silica surface, as is schematically shown in Figure 1. The TEM image of the initial SNs- NH_2 (Figure 1a) is represented along with the particle size histogram (Figure 1b) built by a log-normal distribution using the Sturges method [32]. The average size value obtained for the number of SNs- NH_2 ($N = 290$) is at the level of 54 ± 5 nm (for a confidence level of 0.68). Values of the extracted average size and size dispersity are included in Table 1. The quantity of amino groups per SN determined by the fluorescamine-based luminescent technique [30] is about 6000. The naked (free of amino groups) SNs (50 nm, Figure S2) were also synthesized as the nanobeads for the embedding of Cu^{II} ions with an aim to reveal an impact of the surface-exposed amino groups on the binding of Cu^{II} ions. The phase separation facilitated by the centrifugation was used for washing off the unbound $\text{Cu}(\text{II})$ ions from SNs- $\text{NH}_2\text{-Cu}^{\text{II}}$. The ICP-OES technique was used to determine Si:Cu molar ratios, since such values enable comparing the content of Cu^{II} ions, which is quite different for the SNs and SNs- NH_2 (Table 1). The embedded Cu^{II} ions are manifested by the different spectral patterns in UV-Vis spectra of the dried samples of SNs- Cu^{II} and SNs- $\text{NH}_2\text{-Cu}^{\text{II}}$ (Figure 1c). This, in turn, confirms the difference in both the quantity of the embedded Cu^{II} ions and their coordination environment.

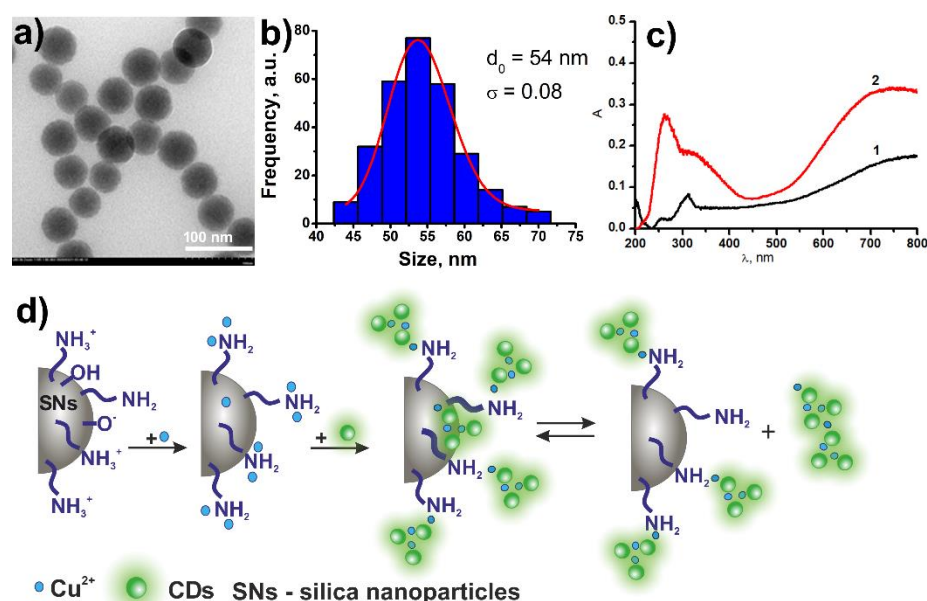


Figure 1. (a) TEM image of SNs- NH_2 ; (b) the particle size histograms and the corresponding curve fitting of sample SNs- NH_2 (d_0 —average diameter, σ —log-normal distribution parameter); (c) UV-Vis/DR spectra of dried samples of SNs- Cu^{II} (1) and SNs- $\text{NH}_2\text{-Cu}^{\text{II}}$ (2); (d) schematic representation of the stepwise synthesis of hybrid nanoparticles SNs- $\text{NH}_2\text{-Cu}^{\text{II}}$ -CDs (silanol groups are presented only at the first step not to complicate the figure).

The DLS and electrokinetic potential (ζ) measurements reveal both positive surface charging and aggregation of SNs- NH_2 (Table 1), since the protonation of the interfacial amino groups recharges the negative charge of the silica surface, but the recharging is insufficient ($\zeta < 30$ mV) to increase the colloidal stability of the nanoparticles. Indeed, both average size and PDI values of SNs- NH_2 are greater than those of SNs. The surface-exposed Si-O^- groups provide the binding sites for Cu^{II} ions, although their binding capacity is much lower than that of the surface-exposed amino groups of SNs- NH_2 . Thus, the binding of SNs with Cu^{II} ions results in the partial surface charge neutralization (compare the ζ -values of SNs and SNs- Cu^{II} in Table 1), but the binding of SNs- NH_2 with Cu^{II} ions results in

recharging of their surface charge (the ζ -values of SNs-NH₂ and SNs-NH₂-Cu^{II} in Table 1). Thus, the efficient binding of Cu^{II} ions via neutral amino groups of SNs-NH₂ restricts their protonation which, in turn, is the reason for the recharging of the corresponding ζ -values from positive to negative.

Table 1. Values of averaged diameter (d^{TEM}) evaluated by TEM method and averaged hydrodynamic diameter (d^{DLS}), polydispersity index (PDI), ζ -potential values and mean peaks (nanoparticle distribution by volume, instead of d^{DLS} at PDI > 0.4) evaluated by DLS technique for different systems, as well as the content of Cu in nanoparticle dispersion (0.1 gL⁻¹) and Si to Cu molar ratio obtained by ICP-OES technique.

System	d^{TEM} , nm	d^{DLS} , nm	PDI	ζ , mV	Mean Peaks, nm	Si:Cu	Content of Cu, mol·L ⁻¹
SNs-NH ₂	55 ± 5	*	0.437	22	220 and 1496	-	-
SNs-NH ₂ -Cu ^{II}	-	*	0.428	-33	231 and 1289	1:0.026	1.7 × 10 ⁻⁵
SNs-NH ₂ -Cu ^{II} -CDs	-	266 ± 9	0.334	-31	-	1:0.005	1.8 × 10 ⁻⁶
SNs	50 ± 5	128 ± 1	0.352	-36	-	-	-
SNs-Cu ^{II}	-	113 ± 2	0.248	-23	-	1:0.007	5 × 10 ⁻⁶
SNs-Cu ^{II} -CDs	-	207 ± 2	0.184	-24	-	1:0 **	**
CDs (C = 0.005 gL ⁻¹)	-	*	0.558	-24	467; 4962	-	-
CDs + 30 μM CuCl ₂	-	*	0.628	-19	3; 602; 3615	-	3 × 10 ⁻⁵
CDs + 300 μM CuCl ₂	-	*	0.627	-15	175; 886; 5203	-	3 × 10 ⁻⁴

* ζ -values and d^{DLS} cannot be accurately evaluated at PDI > 0.4. ** Cu content is too low for evaluation.

The embedding of the CDs on either SNs-NH₂-Cu^{II} or SNs-Cu^{II} was performed through their mixing with the CDs followed by the centrifugation-induced phase separation, as is schematically demonstrated in Figure 1d. The adsorption of the CDs from the aqueous to the nanoparticulate phase becomes evident from the specific green ($\lambda_{\text{em}} = 550$ nm) fluorescence of the redispersed phase (Figure 2a). However, the emission intensity is significantly greater for SNs-NH₂-Cu^{II} than SNs-Cu^{II} after the treating by CDs, while the initial SNs-NH₂ remains nonluminescent after the treating by CDs (Figure 2a). It is worth noting that the phase separation was performed at the instrumental conditions suitable for the phase separation of SNs-NH₂-Cu^{II}, not for the separation of the CDs themselves (for more details see Section 2). The treating of SNs-NH₂-Cu^{II} by the CDs results in the appearance of the green emission characteristic of the CDs (Figure 2a). This strongly suggests the adsorption of the CDs onto SNs-NH₂-Cu^{II}, while no adsorption of the CDs is observed after the similar treating of SNs-NH₂, while the treating of SNs-Cu^{II} is followed by the small but detectable adsorption of the CDs, which is evident from the emission spectra in Figure 2a. Thus, the Cu^{II} ions bound onto the surface of SNs-NH₂-Cu^{II} and SNs-Cu^{II} serve as the anchors for coordinative binding of the CDs. However, the anchoring by the copper ions is greater for SNs-NH₂-Cu^{II} than SNs-Cu^{II}, which is in good agreement with the difference in the binding capacities of Si-O⁻ and amino groups. The step-by-step deposition of copper ions followed by the deposition of the CDs exemplifies the well-known layer-by-layer approach controlled by both kinetic and thermodynamic factors, which is well documented for the layer-by-layer deposition of the oppositely charged polyelectrolytes [33]. It is worth noting that the step-by-step deposition of SNs-NH₂ by Cu^{II} ions and the CDs in a framework of the layer-by-layer synthetic protocol schematically shown in Figure 1d is of key significance in the synthesis of SNs-NH₂-Cu^{II}-CDs. This, in turn, argues for an impact of kinetic rather than thermodynamic control on the synthesis of SNs-NH₂-Cu^{II}-CDs. It is worth assuming that the facilitated by copper ions assemblage of the CDs at the surface of SNs-NH₂-Cu^{II} provides retarding of leaching of the CDs from SNs-NH₂-Cu^{II}-CDs. The concentration and time conditions were optimized in order to provide the balance of high luminescence and stability of SNs-NH₂-Cu^{II}-CDs colloids (Figure S3).

The TEM images of the dried SNs-NH₂-Cu^{II}-CDs colloids confirm the deposition of the CDs onto the silica spheres (Figure S4).

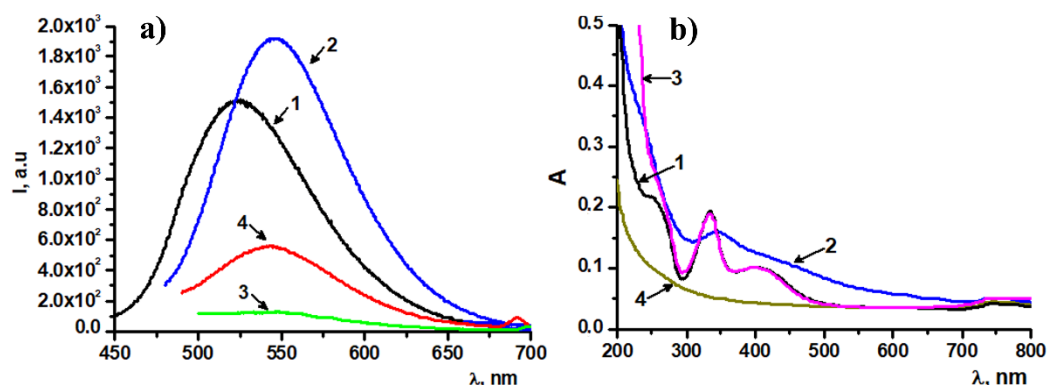


Figure 2. (a) Emission spectra of unbound CDs (1, 0.005 gL^{-1}) and CDs on the surface of SNs-NH₂-Cu^{II} (2, 0.05 gL^{-1}), SNs-NH₂ (3, 0.05 gL^{-1}) and SNs-Cu^{II} (4, 0.05 gL^{-1}) in water; (b) UV-Vis spectra of water dispersion of CDs (1, 0.02 gL^{-1}), SNs-NH₂-Cu^{II}-CDs (2, 0.2 gL^{-1}), Cu^{II}-CDs (3, 1.2 mM of CuCl₂) and SNs-NH₂-Cu^{II} (4, 0.2 gL^{-1}).

Thus, Cu^{II}-facilitated coordination bonds are the main driving forces of the adsorption of the CDs on SNs-NH₂-Cu^{II}. It is worth noting that both SNs-NH₂-Cu^{II} and CDs are negatively surface charged; thus, the embedding of the CDs onto the surface of SNs-NH₂-Cu^{II} takes place through the ion exchange process which, in turn, is driven by the coordinative bonds. However, a lability of coordination bonds in Cu^{II} complexes is a prerequisite for the distribution of Cu^{II} ions between different binding sites provided by the surface-exposed amino groups and the citrate-stabilized CDs. The maximum wavelength red-shifting of the emission of CDs (Figure 2a) confirms their binding with Cu^{II} ions, although the coordination of the Cu^{II} ions with the “free” CDs also cannot be excluded. The aforesaid is a reason for partial washing out of the Cu^{II} ions from SNs-NH₂-Cu^{II} after their treating by the CDs, which is manifested by the changing of Si:Cu ratios from 1:0.026 to 1:0.005.

The coordinative binding of Cu^{II} ions with CDs is the well-known reason for the significant quenching of their fluorescence [15], although the quenching effect depends on the Cu^{II} concentration (Figure S5). Thus, the low Cu^{II} content in SNs-NH₂-Cu^{II}-CDs (Table 1) explains the low quenching effect of Cu^{II} ions as the reason for the high fluorescence (Figure 2a). The developed synthetic protocol includes the phase separation steps providing washing up of the unbound CDs, but the lability of the coordinative binding is the reason for the equilibration between the bound and unbound CDs as it is schematically demonstrated in Figure 1d. The fluorescence of the SNs-NH₂-Cu^{II}-CDs aqueous colloids tends to increase within one day after the synthesis with further invariance within one month at least (Figure S3), which indicates that one day is the time period required for the equilibration of SNs-NH₂-Cu^{II}-CDs with the unbound CDs. The emission band remains invariant within one week at least, while the longer storage for one month results in the back blue-shifting of the band, thus pointing to the disassembly of the CDs from the surface of SNs-NH₂-Cu^{II} (Figure S3).

The electronic absorption of the CDs in aqueous solutions is manifested by two bands at 335 and 405 nm derived from the sp²-carbon-based aromatic systems with different extent of conjugation (Figure 2b), while the shoulder at ~260 nm is derived from the impurities in the as-prepared CDs. The main bands of CDs are red-shifted in the spectrum of SNs-NH₂-Cu^{II}-CDs compared to that of CDs (Figure 2b), while the shoulder at ~260 nm disappears due to washing out of the impurities within the synthesis of SNs-NH₂-Cu^{II}-CDs. Similar bands are revealed in the spectrum of SNs-NH₂-Cu^{II}-CDs (Figure 2b), although they are somewhat red-shifted. The shifting does not derive from the binding with copper ions, since no significant spectral changes are revealed after their addition to the aqueous

CDs colloids (Figure 2b). The latter is rather anticipated since the binding of the CDs with copper ions occurs via the anions and molecules constituting the hydrophilic layer of the CDs, while the red-shifted bands in the spectrum of SNs-NH₂-Cu^{II}-CDs amplify the assemblage of the CDs onto SNs-NH₂-Cu^{II} as a possible reason for the above-mentioned stability of SNs-NH₂-Cu^{II}-CDs. The analysis of the Fourier-transform infrared spectroscopy (FTIR) spectra of CDs and SNs-NH₂-Cu^{II}-CDs indicates the participation of the amide groups of CDs in the binding with SNs-NH₂-Cu^{II}. This is evident from the shifting of the band at 1650 cm⁻¹ associated with the amide group of CDs to ~1720 cm⁻¹ in the spectrum of SNs-NH₂-Cu^{II}-CDs due to the binding of the amide groups with Cu^{II} ions (Figure S6).

3.2. Sensing of GSH by the Fluorescent Response of SNs-NH₂-Cu^{II}-CDs

It is worth anticipating that the above-mentioned quenching effect of Cu^{II} ions on the fluorescence of the CDs (Figure S5) should be a reason for the fluorescence response on the stripping of Cu^{II} ions through their chelation with GSH. Figure 3 demonstrates that the fluorescence of CDs reveals the detectable ability of response to GSH at the specific concentration of Cu^{II} ions (30 μM at least), while SNs-NH₂-Cu^{II}-CDs colloids are able to give the fluorescent response to GSH at the lower concentration level of Cu^{II} ions. It is also worth noting literature data highlighting the diversity of the complexes under mixing of Cu^{II} ions with GSH, including both Cu^{II} and Cu^I ions with GSH and Glutathione disulfide (GSSG) [9]. The fluorescence response of SNs-NH₂-Cu^{II}-CDs is detectable even at the concentration of GSH below 1.0 μM, which corresponds to GSH:Cu molar ratio less than 1:1. Thus, the luminescent response of SNs-NH₂-Cu^{II}-CDs is triggered by GSH-induced complex formation, as the prerequisite for further redox transformations followed by the appearance of Cu^I ions, which are facilitated by the greater molar excess of GSH in regard to Cu^{II} ions [14]. The I/I₀ values tend to linearly increase up to ~12 μM of GSH (Figure 3). The sensitivity can be quantitatively evaluated by the LOD values (for details of the calculation see Section 2), which are 0.15 and 1.65 μM for SNs-NH₂-Cu^{II}-CDs and Cu^{II}-CDs, respectively. The difference indicates that the same amounts of GSH trigger more pronounced disassembly in SNs-NH₂-Cu^{II}-CDs than in Cu^{II}-CDs, arising from the difference in nanoarchitectures of the aforesaid colloids. The LOD value at 0.15 μM is slightly inferior, but at the same order as the LOD values (0.11 [34] and 86 nM [35]) achieved in the sensing of GSH through the emission response of the amino-modified CDs bound with Cu^{II} ions.

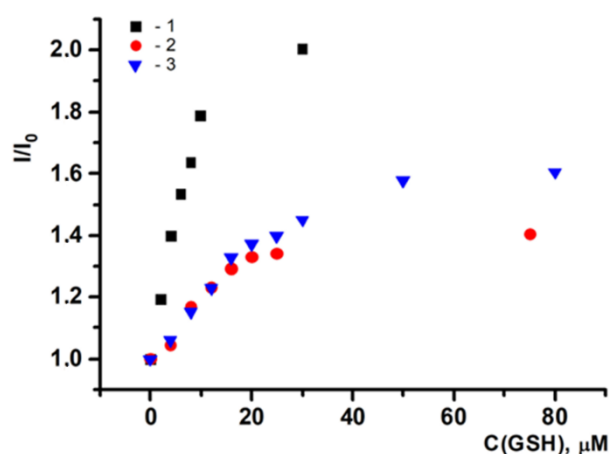
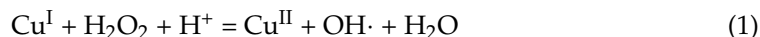


Figure 3. The I/I₀ values (I₀ and I are the fluorescence intensities at 530 nm of SNs-NH₂-Cu^{II}-CDs itself and at different concentrations of GSH) versus GSH concentration in water for SNs-NH₂-Cu^{II}-CDs (1, 0.05 gL⁻¹, 1 μM of Cu^{II}) and Cu^{II}-CDs (2, 3) at 30 μM (2) and 300 μM (3) of CuCl₂ and C_{CD} = 0.005 gL⁻¹.

3.3. ROS Generation

The chemodynamic effect of Cu^{II}-containing nanomaterials is based on the production of hydroxyl radicals through the equilibrium (1). Thus, the reduction of Cu^{II} by glutathione is the prerequisite step for ROS generation.



The ESR technique facilitated by the use of DMPO as the spin traps is a powerful tool in the detection of ROS [36–39], including those generated by copper ions [40]. As has been mentioned above, at least 3-fold molar excess of GSH in regard to Cu^{II} ions is required for the production of Cu^I-(GSH)₂ through the equilibriums (2 and 3), which, in turn, generates OH[·] radicals in the oxygenated aqueous solutions [14].

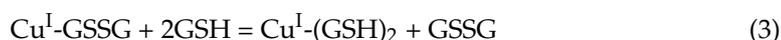


Figure 4a illustrates the rather low intensity of the ESR signals generated by SNs-NH₂-Cu^{II} in aqueous solutions of DMPO. The arrows demonstrate the insignificant level of the signals derived from the DMPO-OH[·] adducts [41], while the other ones most probably arise from the trace amounts of copper-initiated oxidized forms of DMPO, although the designation of their nature lies out of the scope of the present work due to their low intensity. The addition of GSH (50 μM) to SNs-NH₂-Cu^{II} in 5:1 GSH:Cu concentration ratio suppresses all weak signals generated by SNs-NH₂-Cu^{II} in the solution of DMPO (Figure 4a), while the signals peculiar for DMPO-OH[·] adduct grow under the addition of GSH (350 μM) resulting in the GSH:Cu ratio 35:1, although the intensity of the signals comes to the detectable level after the gentle heating of the sample from 22 to 38 °C (Figure S7 and Figure 4). This fact confirms the impact of the reductive potential of GSH on the ROS generation in the Cu^{II}-based nanomaterials.

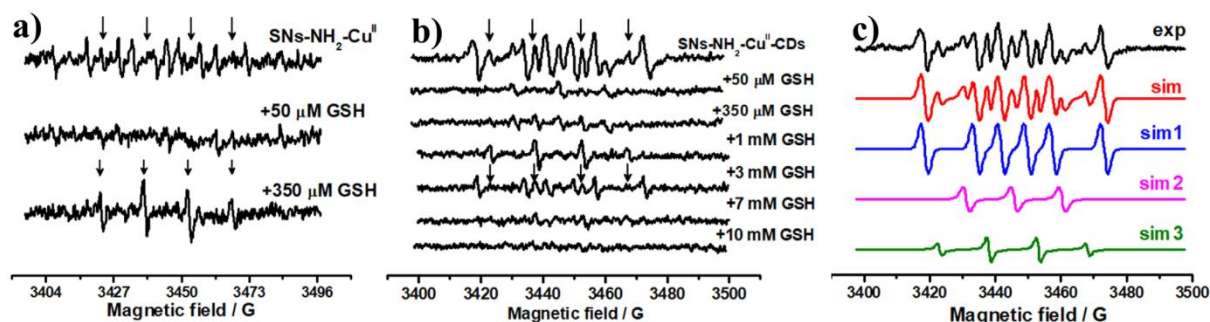


Figure 4. ESR signals of aqueous dispersions of SNs-NH₂-Cu^{II} (a) and SNs-NH₂-Cu^{II}-CDs (b) (0.5 gL⁻¹; 10 μM of Cu^{II}) in the presence of GSH at 50 μM, 350 μM, 1 mM, 3 mM, 7 mM and 10 mM with DMPO spin trap (0.1 M); DMPO-OH[·] signal positions are shown by arrows. In addition, experimental (exp) and simulated (sim) ESR signal of Cu^{II}-CDs (10 μM of Cu^{II} and 0.5 gL⁻¹ of CDs) and SNs-NH₂-Cu^{II}-CDs colloids (c); ESR signal is the interference of DMPO-X[·] spin-adducts (sim1), an oxidized DMPO radical (sim2) and DMPO-OH[·] spin-adducts (sim3). The experimental spectra were recorded at 38 °C.

The ESR technique reveals the generation of the detectable aggregate signals in the aqueous colloids of SNs-NH₂-Cu^{II}-CDs themselves; the intensity of the bands also tends to increase with the temperature growth from 22 to 38 °C (Figure S7 and Figure 4b). The aggregate nature of the signals results from the interference of DMPO-OH[·] and DMPO-X[·] (X[·] denotes the methyl and alkoxy radicals [42]), as is clear from the simulation and summarizing of DMPO-OH[·] and DMPO-X[·] signals shown in Figure 4c. The aqueous colloids of the CDs generate a similar spectral pattern in the presence of Cu^{II} ions at 38 °C

(Figure 4b,c). The aforesaid indicates that the combination of the green-emitting CDs with Cu^{II} ions is the prerequisite for the self-boosting generation of $\text{OH}\cdot$ and $\text{X}\cdot$ radicals. The potential of the green-emitting CDs to reduce Cu^{II} is derived from the complex nature of the CDs constructed from carbon atoms at different oxidation states from 0 to +4. The low oxidation states of carbon are the prerequisite for their reductive potential, since the ability of carbon and carbon oxide to reduce CuO to Cu_2O is well known [43]. The already documented examples of the sensing of bromate in aqueous solutions due to the reductive potential of CDs also argue for the aforesaid tendency [12]. Thus, the reductive potential of the CDs is the reason for the production of Cu^{I} complexes, which in turn generate $\text{OH}\cdot$ and $\text{X}\cdot$ radicals.

The addition of GSH up to the level of 350 μM to $\text{SNs-NH}_2\text{-Cu}^{\text{II}}\text{-CDs}$ quenches the already generated $\text{DMPO-OH}\cdot$ and $\text{DMPO-X}\cdot$ signals at 22 °C since the radicals are taken up by GSH due to its efficient scavenger function deriving from the easy transformation into GSSG [14]. However, the heating of the sample to 38 °C generates the signal of $\text{DMPO-OH}\cdot$ adducts (Figure 4b) without any contribution of $\text{DMPO-X}\cdot$ adduct signals. The increased amounts of GSH (1.0 mM) intensify the signals of $\text{DMPO-OH}\cdot$ spin-adducts, while the intensity of the signals gradually decreases with further increase in the concentration to 3 and 7 mM and disappears at 10.0 mM GSH, even at 38 °C (Figure 4b). This indicates that the production of Cu^{I} ions due to the reductive function of GSH is predominant at the concentration level of 350 μM –1 mM. However, the scavenger effect of GSH increases with further concentration growth, being predominant when the concentration level of GSH reaches 10 mM. Taking into account that the intracellular level of GSH varies within 1–10 mM, being greater in cancer cells than in normal cells [44,45], the cytotoxic effect of $\text{SNs-NH}_2\text{-Cu}^{\text{II}}\text{-CDs}$ should be greatly affected by the nature of cells. Moreover, the temperature variation in the physiological range (37–40 °C) should be noted as the factor affecting the ROS generation by $\text{SNs-NH}_2\text{-Cu}^{\text{II}}\text{-CDs}$ colloids under their cell internalization.

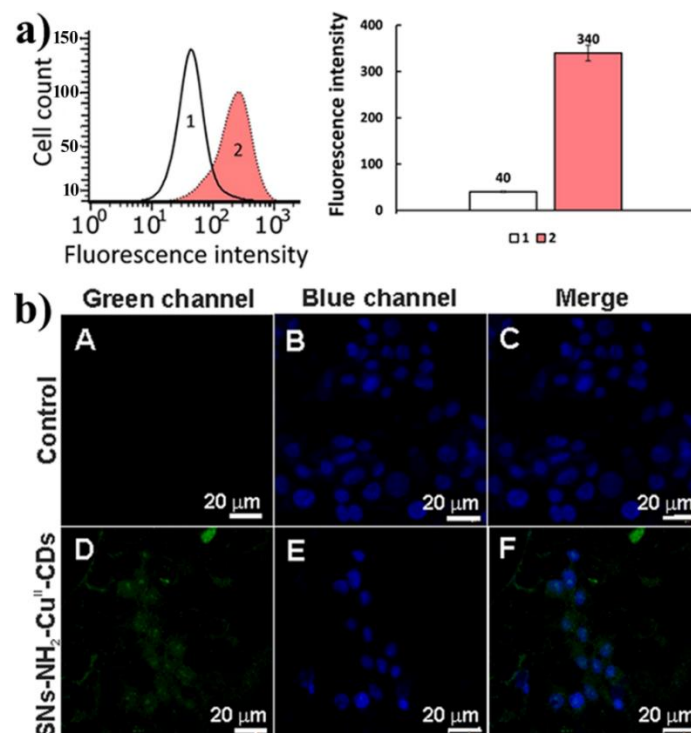
3.4. Cell Internalization of $\text{SNs-NH}_2\text{-Cu}^{\text{II}}\text{-CDs}$ and Its Effect on Cell Viability

The amino-decorated SNs commonly demonstrate good cell internalization [46,47], although the surface decoration of nanoparticles plays an essential role in their interactions with cells [48]. The cell internalization of CDs [49–52] is very efficient; thus, $\text{SNs-NH}_2\text{-Cu}^{\text{II}}\text{-CDs}$ with the surface-exposed CDs can demonstrate perfect cellular uptake behavior. The cell viability after the incubation with $\text{SNs-NH}_2\text{-Cu}^{\text{II}}\text{-CDs}$ and $\text{SNs-NH}_2\text{-Cu}^{\text{II}}$ was measured for M-HeLa and Chang Liver cell lines prior to flow cytometry measurements, and the results are shown in Table 2. The results presented in Table 2 indicate that the cell viability values are no less than 60% even at 1 gL^{-1} . This clearly demonstrates the very low cytotoxic effect of $\text{SNs-NH}_2\text{-Cu}^{\text{II}}\text{-CDs}$ on the cell viability of M-HeLa and Chang Liver standard cell lines, with the IC_{50} value above 1 gL^{-1} (Table 2). It is worth noting that such a high IC_{50} value is comparable with the cytotoxicity of the naked silica nanoparticles [53].

Both flow cytometry data and fluorescence microscopy imaging reveal efficient cellular uptake behavior of $\text{SNs-NH}_2\text{-Cu}^{\text{II}}\text{-CDs}$ (Figures 5a and S8). The staining of an intracellular space by the “free” CDs is commonly limited by poor entry to the cell nuclei [49–51]. The confocal microscopy images of the cells incubated by $\text{SNs-NH}_2\text{-Cu}^{\text{II}}\text{-CDs}$ colloids indicate the cytoplasmatic localization of the colloids, with some entering into the cell nuclei (Figure 5b), while the confocal images of M-HeLa cells after the incubation by the CDs indicate a rather poor staining of the cell nuclei (Figure S9). The revealed specificity of $\text{SNs-NH}_2\text{-Cu}^{\text{II}}\text{-CDs}$ in the cell internalization does not result in a detectable effect on the cell viability (Table 2). This may be due to the high intracellular level of GSH, although further widening of cell lines with different intracellular levels of GSH is required to argue for or against this assumption.

Table 2. The cell viability and IC₅₀ values of M-HeLa and Chang Liver cells in the presence of different concentrations of SNs-NH₂-Cu^{II}-CDs and SNs-NH₂-Cu^{II}.

Compound	Concentration, gL ⁻¹	M-HeLa		Chang Liver	
		Cell Viability,%	IC ₅₀	Cell Viability,%	IC ₅₀
SNs-NH ₂ -Cu ^{II} -CDs	1	71.3	>1 gL ⁻¹	62.2	>1 gL ⁻¹
	0.5	79.3		64.4	
	0.25	82.5		74.5	
	0.125	100		79.4	
	0.0625	100		83.8	
	0.0313	100		87.9	
SNs-NH ₂ -Cu ^{II}	1	69.3	>1 gL ⁻¹	63.8	>1 gL ⁻¹
	0.5	75.13		67.4	
	0.25	76.3		78.9	
	0.125	79.1		79.1	
	0.0625	100		82.3	
	0.0313	100		89.8	

**Figure 5.** (a) Cellular uptake study: 1—Control; 2—SNs-NH₂-Cu^{II}-CDs (0.5 gL⁻¹). (b) Confocal laser microscopy images of the control M-Hela cell lines (A–C) and cells incubated with SNs-NH₂-Cu^{II}-CDs (D–F) at 0.5 gL⁻¹ stained with DAPI.

The cell viability of M-HeLa cells is insignificantly affected by both SNs-NH₂-Cu^{II}-CDs and SNs-NH₂-Cu^{II} (Table 2). This can be explained by the predominance of the scavenger effect compared to the reductive effect of GSH, which in turn is dependent on its intracellular level, although wider cell line variation is required for revealing an impact of the cell lines on the cytotoxicity of SNs-NH₂-Cu^{II}-CDs. Nevertheless, the represented results for the first time introduce the proof of concept of the use of Cu^{II}-based coordinative bonds as the driving force of both the assemblage of CDs at the surface of SNs-NH₂ and self-boosting ROS generation. It is also demonstrated that the Cu^{II}-facilitated surface decoration of SNs-NH₂ by the green-emitting CDs provides the basis for stimuli-responsive

fluorescence, which along with the spin-trap-facilitated ESR technique enables highlighting the impact of GSH concentration on the predominance of different functions of GSH, such as complex formation, scavenger of radicals and reducing agent.

4. Conclusions

In summary, the present report highlights the coordinative bonds as the driving forces of the self-assembly of green-emitting CDs facilitated by Cu^{II} ions at the surface of amino-modified silica nanoparticles (SNs-NH₂), resulting in the SNs-NH₂-Cu^{II}-CDs aqueous colloids. The green fluorescence of the CDs incorporated into SNs-NH₂-Cu^{II}-CDs is somewhat quenched and red-shifted compared to that of the unbound CDs, which results from their coordinative binding with Cu^{II} ions. The fluorescence of SNs-NH₂-Cu^{II}-CDs is contributed by the assembled and the unbound CDs equilibrated with each other. The removal of Cu^{II} ions from SNs-NH₂-Cu^{II}-CDs due to their chelating with GSH destroys the Cu^{II} -facilitated assemblage of CDs, leading to the growing extent of the unbound CDs. This, in turn, is manifested by the blue-shifting and enhancement of the fluorescence band, which enables sensing GSH with the LOD value at 0.15 μM . The spin-trap-facilitated ESR technique was applied to reveal the chemodynamic activity of SNs-NH₂-Cu^{II} and SNs-NH₂-Cu^{II}-CDs aqueous colloids themselves and in the presence of different amounts of GSH. The results for the first time demonstrate the self-boosting generation of hydroxyl ($\text{OH}\cdot$), alkyl and alkoxy ($\text{X}\cdot$) radicals by SNs-NH₂-Cu^{II}-CDs. The revealed tendencies highlight the reductive potential of the CDs as the reason for the generation of $\text{OH}\cdot$ and $\text{X}\cdot$ in the aqueous colloids of SNs-NH₂-Cu^{II}-CDs, which is enhanced with the temperature rise within 22–40 °C. The ESR measurements at different concentrations of GSH reveal the different effects of GSH, namely quenching of the radical species at 5:1 GSH:Cu molar ratio and generation of $\text{OH}\cdot$ radicals at the ratio above 100:1, while the generation of $\text{OH}\cdot$ and $\text{X}\cdot$ ceases when the ratio reaches 1000:1. This highlights the concentration conditions optimal for scavenger and reductive potentials of GSH. The flow cytometry and fluorescence and confocal microscopy methods revealed the specificity in the cell internalization and intracellular localization of SNs-NH₂-Cu^{II}-CDs in comparison with those of the carbon dots themselves. The low cytotoxic effects of both SNs-NH₂-Cu^{II}-CDs and SNs-NH₂-Cu^{II} on the cell viability of M-HeLa and Chang Liver cell lines can be explained by the intracellular level of GSH being sufficient for the predominance of its scavenger effect.

Supplementary Materials: The following supporting information can be downloaded at: <https://www.mdpi.com/article/10.3390/coatings12010097/s1>, Figure S1. (a) The emission spectra of fluorophore, obtained from interaction of fluorescamine (0.55 mM) with various concentrations of alanine (1— 1.6×10^{-7} , 2— 1×10^{-6} , 3— 2.5×10^{-6} , 4— 4×10^{-6} , 5— 5.5×10^{-2}), SNs-NH₂ (6) (0.05 gL^{-1}), at 0.025 M borate buffer pH = 9, $\lambda_{\text{ex}} = 390 \text{ nm}$; (b) the calibration graphic; Figure S2. TEM-image of SNs; Figure S3. The emission spectra of water dispersion of SNs-NH₂-Cu^{II}-CDs (0.5 gL^{-1}): (a) prepared by mixing of water dispersions of SNs-NH₂-Cu^{II} and CDs at different concentration ratios (SNs:CDs) designated on the graphic, after 1 day of storage; (b) SNs-NH₂-Cu^{II}-CDs prepared at SNs:CDs=1:20 after various period of time of this system storage (also designated on the graphic). $\lambda_{\text{ex}} = 420 \text{ nm}$, slit = 5 nm, voltage = 500 mV; Figure S4. TEM-image of SNs-NH₂-Cu^{II}-CDs, where SNs are manifested by the larger silica spheres, while the CDs as black dots on their surface; Figure S5. The dependence of the emission intensity of CDs (0.005 gL^{-1}) on the concentration of CuCl_2 in water; $\lambda_{\text{ex}} = 420 \text{ nm}$, slit = 5 nm, voltage = 700 mV. The emission intensity was normalized to initial luminescent intensity of CDs before addition of water solution of CuCl_2 ; Figure S6. The Infrared spectrum of CDs (black) and SNs-NH₂-Cu^{II}-CDs (blue); Figure S7. The ESR spectra of SNs-NH₂-Cu^{II}-CDs (0.5 gL^{-1} ; 10 μM of Cu^{II}) in the presence of GSH at 50, 350 and 1000 μM with DMPO spin trap (0.1 M) at 22 °C; Figure S8. Fluorescent microscopy images of M-HeLa cells incubated with SNs-NH₂-Cu^{II}-CDs at 0.5 gL^{-1} (Nikon eclipse Ci, $\times 1000$ oil); Figure S9. Confocal laser microscopy images of the control M-HeLa cell lines (A–C) and cells, incubated with CDs (D–F) at 0.5 gL^{-1} stained with DAPI.

Author Contributions: Conceptualization, A.M.; Investigation, O.B., A.D. (Alexey Dovjenko), K.K., R.B., I.N., A.L. (Artem Laskin), A.V., A.L. (Anna Lyubina), S.A., T.G., A.D. (Amina Daminova) and

V.E.; Resources, R.Z. and S.F.; Supervision, A.M.; Visualization, O.B., A.D. (Alexey Dovjenko), R.B. and A.V.; Writing—original draft, A.D. (Alexey Dovjenko) and K.K.; Writing—review and editing, O.B. and A.M. All authors have read and agreed to the published version of the manuscript.

Funding: Authors gratefully acknowledge RFBR and CNR, Grant No. 20-53-7802A for financial support.

Institutional Review Board Statement: Not applicable.

Informed Consent Statement: Not applicable.

Data Availability Statement: Data sharing is not applicable to this article.

Acknowledgments: Authors gratefully acknowledge Assigned Spectral-Analytical Center of FRC Kazan Scientific Center of RAS for providing necessary facilities to carry out physical-chemical measurements.

Conflicts of Interest: The authors declare no conflict of interest.

References

1. Lucena, R.; Simonet, B.M.; Cárdenas, S.; Valcárcel, M. Potential of nanoparticles in sample preparation. *J. Chromatogr. A* **2011**, *1218*, 620–637. [[CrossRef](#)] [[PubMed](#)]
2. Calabrese, C.; Parola, V.L.; Testa, M.L.; Liotta, L.F. Antifouling and antimicrobial activity of Ag, Cu and Fe nanoparticles supported on silica and titania. *Inorg. Chim. Acta* **2022**, *529*, 120636. [[CrossRef](#)]
3. Shibu, E.S.; Hamada, M.; Murase, N.; Biju, V. Nanomaterials formulations for photothermal and photodynamic therapy of cancer. *J. Photochem. Photobiol. C Photochem. Rev.* **2013**, *15*, 53–72. [[CrossRef](#)]
4. Zhong, W. Nanomaterials in fluorescence-based biosensing. *Anal. Bioanal. Chem.* **2009**, *394*, 47–59. [[CrossRef](#)]
5. Cao, L.; Wang, X.; Meziani, M.J.; Lu, F.; Wang, H.; Luo, P.G.; Lin, Y.; Harruff, B.A.; Veca, L.M.; Murray, D.; et al. carbon dots for multiphoton bioimaging. *J. Am. Chem. Soc.* **2007**, *129*, 11318–11319. [[CrossRef](#)]
6. Baker, S.N.; Baker, G.A. Luminescent carbon nanodots: Emergent nanolights. *Angew. Chem. Int. Ed.* **2010**, *49*, 6726–6744. [[CrossRef](#)]
7. Liu, J.; Rehman, S.; Fu, Z.; Liu, Y.; Lu, Y.; Bi, H.; Morais, P.C. Room-temperature multiferroicity in magnetic field-poled polyaniline and its enhancement via Cu²⁺-complexation. *Synth. Met.* **2019**, *253*, 131–140. [[CrossRef](#)]
8. Wieszczycka, K.; Staszak, K.; Wozniak-Budych, M.J.; Litowczenko, J.; Maciejewska, B.M.; Jurga, S. Surface functionalization—The way for advanced applications of smartmaterials. *Coord. Chem. Rev.* **2021**, *436*, 2138462. [[CrossRef](#)]
9. Choudhury, N.; Saha, B.; De, P. Recent progress in polymer-based optical chemosensors for Cu²⁺ and Hg²⁺ Ions: A comprehensive review. *Eur. Polym. J.* **2021**, *145*, 110233. [[CrossRef](#)]
10. Ghaferi, M.; Esfahani, M.K.M.; Raza, A.; Harthi, S.A.; Shahmabadi, H.E.; Alavi, S.E. Mesoporous silica nanoparticles: Synthesis methods and their therapeutic use-recent advances. *J. Drug Target.* **2021**, *29*, 131–154. [[CrossRef](#)]
11. Sarker, M.Z.; Rahman, M.M.; Minami, H.; Suzuki, T.; Hossain, M.K.; Ahmad, H. Mesoporous amine functionalized SiO₂ supported Cu nanocatalyst and a kinetic-mechanistic degradation study of azo dyes. *Colloids Surf. A Physicochem. Eng. Asp.* **2021**, *617*, 126403. [[CrossRef](#)]
12. Xiang, G.; Fan, H.; Zhang, H.; He, L.; Jiang, X.; Zhao, W. Carbon dot doped silica nanoparticles as fluorescent probe for determination of bromate in drinking water samples. *Can. J. Chem.* **2018**, *96*, 24–29. [[CrossRef](#)]
13. Zhao, S.; Sun, S.; Jiang, K.; Wang, Y.; Liu, Y.; Wu, S.; Li, Z.; Shu, Q.; Lin, H. In Situ Synthesis of Fluorescent Mesoporous Silica–Carbon Dot Nanohybrids Featuring Folate Receptor-Overexpressing Cancer Cell Targeting and Drug Delivery. *Nano-Micro Lett.* **2019**, *11*, 32. [[CrossRef](#)]
14. Aliaga, M.E.; López Alarcón, C.; Bridi, R.; Speisky Cosoy, H. Redox-implications associated with the formation of complexes between copper ions and reduced or oxidized glutathione. *J. Inorg. Biochem.* **2016**, *154*, 78–88. [[CrossRef](#)]
15. Sun, S.; Chen, Q.; Tang, Z.; Liu, C.; Li, Z.; Wu, A.; Lin, H. Tumor microenvironment stimuli-responsive fluorescence imaging and synergistic cancer therapy by carbon-dot–Cu²⁺ nanoassemblies. *Angew. Chem. Int. Ed.* **2020**, *59*, 2–10. [[CrossRef](#)]
16. Połec-Pawlak, K.; Ruzik, R.; Lipiec, E. Investigation of Cd(II), Pb(II) and Cu(I) complexation by glutathione and its component amino acids by ESI-MS and size exclusion chromatography coupled to ICP-MS and ESI-MS. *Talanta* **2007**, *72*, 1564–1572. [[CrossRef](#)]
17. Xu, M.; Yang, G.; Bi, H.; Xu, J.; Feng, L.; Yang, D.; Sun, Q.; Gai, S.; He, F.; Dai, Y.; et al. Combination of CuS and g-C₃N₄ QDs on upconversion nanoparticles for targeted photothermal and photodynamic cancer therapy. *Chem. Eng. J.* **2019**, *360*, 866–878. [[CrossRef](#)]
18. Ma, B.; Wang, S.; Liu, F.; Zhang, S.; Duan, J.; Li, Z.; Kong, Y.; Sang, Y.; Liu, H.; Bu, W.; et al. Self-Assembled Copper–Amino Acid Nanoparticles for in Situ Glutathione “AND” H₂O₂ Sequentially Triggered Chemodynamic Therapy. *J. Am. Chem. Soc.* **2019**, *141*, 849–857. [[CrossRef](#)]
19. Cao, S.; Li, X.; Gao, Y.; Li, F.; Li, K.; Cao, X.; Dai, Y.; Mao, L.; Wang, S.; Tai, X. A simultaneously GSH-depleted bimetallic Cu(ii) complex for enhanced chemodynamic cancer therapy. *Dalton Trans.* **2020**, *49*, 11851–11858. [[CrossRef](#)]

20. Wu, H.; Chen, F.; Gu, D.; You, C.; Sun, B. A pH-activated autocatalytic nanoreactor for self-boosting Fenton-like chemodynamic therapy. *Nanoscale* **2020**, *12*, 17319–17331. [[CrossRef](#)]
21. Nikam, A.N.; Pandey, A.; Fernandes, G.; Kulkarni, S.; Mutalik, S.P.; Padya, B.S.; George, S.D.; Mutalik, S. Copper sulphide based heterogeneous nanoplatforams for multimodal therapy and imaging of cancer: Recent advances and toxicological perspectives. *Coord. Chem. Rev.* **2020**, *419*, 213356. [[CrossRef](#)]
22. Wang, X.; Zhong, X.; Liu, Z.; Cheng, L. Recent progress of chemodynamic therapy-induced combination cancer therapy. *Nano Today* **2020**, *35*, 100946. [[CrossRef](#)]
23. Yang, B.; Chen, Y.; Shi, J. Reactive Oxygen Species (ROS)-Based Nanomedicine. *Chem. Rev.* **2019**, *119*, 4881–4985. [[CrossRef](#)]
24. Zhong, Y.; Li, X.; Chen, J.; Wang, X.; Wei, L.; Fang, L.; Kumar, A.; Zhuang, S.; Liu, J. Recent advances in MOF-based nanoplatforams generating reactive species for chemodynamic therapy. *Dalton Trans.* **2020**, *49*, 11045–11058. [[CrossRef](#)]
25. Hu, J.; Liu, S. Modulating intracellular oxidative stress via engineered nanotherapeutics. *J. Control. Release* **2020**, *319*, 333–343. [[CrossRef](#)]
26. Wang, W.; Zhang, Q.; Zhang, M.; Liu, Y.; Shen, J.; Zhou, N.; Lua, X.; Zhao, C. Multifunctional red carbon dots: A theranostic platform for magnetic resonance imaging and fluorescence imaging-guided chemodynamic therapy. *Analyst* **2020**, *145*, 3592–3597. [[CrossRef](#)]
27. Zholobak, N.M.; Popov, A.L.; Shcherbakov, A.B.; Popova, N.R.; Guzyk, M.M.; Antonovich, V.P.; Yegorova, A.V.; Scrypynets, Y.V.; Leonenko, I.I.; Baranchikov, A.Y.; et al. Facile fabrication of luminescent organic dots by thermolysis of citric acid in urea melt, and their use for cell staining and polyelectrolyte microcapsule labelling. *Beilstein J. Nanotechnol.* **2016**, *7*, 1905–1917. [[CrossRef](#)] [[PubMed](#)]
28. Liu, S.; Zhang, H.-L.; Liu, T.-C.; Liu, B.; Cao, Y.-C.; Huang, Z.-L.; Zhao, Y.-D.; Luo, Q.-M. Optimization of methods for introduction of amine groups onto the silica nanoparticle surface. *J. Biomed. Mater. Res.* **2007**, *80A*, 752–757. [[CrossRef](#)] [[PubMed](#)]
29. Mustafina, A.R.; Fedorenko, S.V.; Konovalova, O.D.; Menshikova, A.Y.; Shevchenko, N.N.; Soloveva, S.E.; Konovalov, A.I.; Antipin, I.S. Novel Highly Charged Silica-Coated Tb(III) Nanoparticles with Fluorescent Properties Sensitive to Ion Exchange and Energy Transfer Processes in Aqueous Dispersions. *Langmuir* **2009**, *25*, 3146–3151. [[CrossRef](#)] [[PubMed](#)]
30. Chen, Y.; Zhang, Y. Fluorescent quantification of amino groups on silica nanoparticle surfaces. *Anal. Bioanal. Chem.* **2011**, *399*, 2503–2509. [[CrossRef](#)] [[PubMed](#)]
31. Sharipova, R.R.; Belenok, M.G.; Garifullin, B.F.; Sapunova, A.S.; Voloshina, A.D.; Andreeva, O.V.; Strobyskina, I.Y.; Skvortsova, P.V.; Zuev, Y.F.; Kataev, V.E. Synthesis and anti-cancer activities of glycosides and glycoconjugates of diterpenoid isosteviol. *Med. Chem. Comm.* **2019**, *10*, 1488–1498. [[CrossRef](#)]
32. Aragon, F.H.; Coaquira, J.A.H.; Villegas-Lelovsky, L.; Silva, S.W.; Cesar, D.F.; Nagamine, L.C.C.M.; Cohen, R.; Menéndez-Proupin, E.; Morais, P.C. Evolution of the doping regimes in the Al-doped SnO₂ nanoparticles prepared by a polymer precursor method. *J. Phys. Cond. Matter* **2015**, *27*, 095301. [[CrossRef](#)]
33. Sukhishvili, S.A.; Kharlampieva, E.; Izumrudov, V. Where polyelectrolyte multilayers and polyelectrolyte complexes meet. *Macromolecules* **2006**, *39*, 8873–8881. [[CrossRef](#)]
34. Yang, R.; Guo, X.; Jia, L.; Zhang, Y. A fluorescent “on-off-on” assay for selective recognition of Cu(II) and glutathione based on modified carbon nanodots, and its application to cellular imaging. *Microchim. Acta* **2017**, *184*, 1143–1150. [[CrossRef](#)]
35. Guo, Y.; Yang, L.; Li, W.; Wang, X.; Shang, Y.; Li, B. Carbon dots doped with nitrogen and sulfur and loaded with copper(II) as a “turn-on” fluorescent probe for cystein, glutathione and homocysteine. *Microchim. Acta* **2016**, *183*, 1409–1416. [[CrossRef](#)]
36. Elistratova, J.; Mukhametshina, A.; Kholin, K.; Nizameev, I.; Mikhailov, M.; Sokolov, M.; Khairullin, R.; Miftakhova, R.; Shammas, G.; Kadirov, M.; et al. Interfacial uploading of luminescent hexamolybdenum cluster units onto amino-decorated silica nanoparticles as new design of nanomaterial for cellular imaging and photodynamic therapy. *J. Colloid Interface Sci.* **2019**, *538*, 387–396. [[CrossRef](#)]
37. Fedorenko, S.; Elistratova, J.; Stepanov, A.; Khazieva, A.; Mikhailov, M.; Sokolov, M.; Kholin, K.; Nizameev, I.; Mendes, R.; Rümmele, M.; et al. ROS-generation and cellular uptake behavior of amino-silica nanoparticles arisen from their uploading by both iron-oxides and hexamolybdenum clusters. *Mater. Sci. Eng. C* **2020**, *117*, 1113052. [[CrossRef](#)]
38. Abbas, K.; Babić, N.; Peyrot, F. Use of spin traps to detect superoxide production in living cells by electron paramagnetic resonance (EPR) spectroscopy. *Methods* **2016**, *109*, 31–43. [[CrossRef](#)]
39. Carini, M.; Aldini, G.; Orioli, M.; Facino, R. Electron paramagnetic resonance (EPR) spectroscopy: A versatile and powerful tool in pharmaceutical and biomedical analysis. *Curr. Pharm. Anal.* **2006**, *2*, 141–159. [[CrossRef](#)]
40. Angelé-Martínez, C.; Nguyen, K.V.T.; Ameer, F.S.; Anker, J.N.; Brumaghim, J.L. Reactive oxygen species generation by copper(II) oxide nanoparticles determined by DNA damage assays and EPR spectroscopy. *Nanotoxicology* **2017**, *11*, 278–288. [[CrossRef](#)]
41. Hedrick, W.R.; Webb, M.D.; Zimbrick, J.D. Spin trapping of reactive uracyl radicals produced by ionizing radiation in aqueous solutions. *Inter. J. Radiat. Biol. Relat. Stud. Phys. Chem. Med.* **1982**, *41*, 435–442. [[CrossRef](#)]
42. Kirino, Y.; Ohkuma, T.; Kwan, T. Spin trapping with 5,5-dimethylpyrroline-N-oxide in aqueous solution. *Chem. Pharm. Bull.* **1981**, *29*, 29–34. [[CrossRef](#)]
43. Liu, L.; Zhang, T.J.; Cui, K.; Dong, Y.D. Reduction of copper oxide with graphite by mechanical alloying. *J. Mater. Res.* **1999**, *14*, 4062–4069. [[CrossRef](#)]

44. Jiang, C.; Zhang, C.; Song, J.; Ji, X.; Wang, W. Cytidine-gold nanoclusters as peroxidase mimetic for colorimetric detection of glutathione (GSH), glutathione disulfide (GSSG) and glutathione reductase (GR). *Spectrochim. Acta Part A Mol. Biomol. Spectrosc.* **2021**, *250*, 119316. [[CrossRef](#)]
45. Xiong, Y.; Xiao, C.; Li, Z.; Yang, X. Engineering nanomedicine for glutathione depletion-augmented cancer therapy. *Chem. Soc. Rev.* **2021**, *50*, 6013. [[CrossRef](#)]
46. Shahabi, S.; Treccani, L.; Dringen, R.; Rezwani, K. Modulation of Silica Nanoparticle Uptake into Human Osteoblast Cells by Variation of the Ratio of Amino and Sulfonate Surface Groups: Effects of Serum. *ACS Appl. Mater. Interfaces* **2015**, *7*, 13821–13833. [[CrossRef](#)]
47. Fedorenko, S.V.; Mustafina, A.R.; Mukhametshina, A.R.; Jilkin, M.E.; Mukhametzyanov, T.A.; Solovieva, A.O.; Pozmogova, T.N.; Shestopalova, L.V.; Shestopalov, M.A.; Kholin, K.V.; et al. Cellular imaging by green luminescence of Tb(III)-doped aminommodified silica nanoparticles. *Mater. Sci. Eng. C* **2017**, *76*, 551–558. [[CrossRef](#)]
48. Verma, A.; Stellacci, F. Effect of Surface Properties on Nanoparticle–Cell Interactions. *Small* **2010**, *6*, 12–21. [[CrossRef](#)]
49. Li, Q.; Ohulchanskyy, T.Y.; Liu, R.; Koynov, K.; Wu, D.; Best, A.; Kumar, R.; Bonoiu, A.; Prasad, P.N. Photoluminescent carbon dots as biocompatible nanoprobe for targeting cancer cells in vitro. *J. Phys. Chem. C* **2010**, *114*, 12062–12068. [[CrossRef](#)]
50. Zhu, S.; Zhang, J.; Qiao, C.; Tang, S.; Li, Y.; Yuan, W.; Li, B.; Tian, L.; Liu, F.; Hu, R.; et al. Strongly green-photoluminescent graphene quantum dots for bioimaging applications. *Chem. Commun.* **2011**, *47*, 6858–6860. [[CrossRef](#)]
51. Su, W.; Wu, H.; Xu, H.; Zhang, Y.; Li, Y.; Li, X.; Fan, L. Carbon dots: A booming material for biomedical applications. *Mater. Chem. Front.* **2020**, *4*, 821–836. [[CrossRef](#)]
52. Harush-Frenkel, O.; Debotton, N.; Benita, S.; Altschuler, Y. Targeting of nanoparticles to the clathrin-mediated endocytic pathway. *Biochem. Biophys. Res. Commun.* **2007**, *353*, 26–32. [[CrossRef](#)] [[PubMed](#)]
53. Zhu, J.; Liao, L.; Zhu, L.; Zhang, P.; Guo, K.; Kong, J.; Ji, C.; Liu, B. Size-dependent cellular uptake efficiency, mechanism, and cytotoxicity of silica nanoparticles toward HeLa cells. *Talanta* **2013**, *107*, 408–415. [[CrossRef](#)] [[PubMed](#)]